PCCP

PAPER

View Article Online
View Journal | View Issue

Cite this: *Phys. Chem. Chem. Phys.*, 2014, **16**, 25161

Electrical conductivity of activated carbon–metal oxide nanocomposites under compression: a comparison study

A. Barroso-Bogeat,*[a] M. Alexandre-Franco,[a] C. Fernández-González,[a] A. Macías-García[b] and V. Gómez-Serrano[a]

Received 3rd September 2014,
Accepted 2nd October 2014

DOI: 10.1039/c4cp03952a

www.rsc.org/pccp

From a granular commercial activated carbon (AC) and six metal oxide (Al_2O_3, Fe_2O_3, SnO_2, TiO_2, WO_3 and ZnO) precursors, two series of AC–metal oxide nanocomposites were prepared by wet impregnation, oven-drying at 120 °C, and subsequent heat treatment at 200 or 850 °C in an inert atmosphere. Here, the electrical conductivity of the resulting products was studied under moderate compression. The influence of the applied pressure, sample volume, mechanical work, and density of the hybrid materials was thoroughly investigated. The DC electrical conductivity of the compressed samples was measured at room temperature by the four-probe method. Compaction assays suggest that the mechanical properties of the nanocomposites are largely determined by the carbon matrix. Both the decrease in volume and the increase in density were relatively small and only significant at pressures lower than 100 kPa for AC and most nanocomposites. In contrast, the bulk electrical conductivity of the hybrid materials was strongly influenced by the intrinsic conductivity, mean crystallite size, content and chemical nature of the supported phases, which ultimately depend on the metal oxide precursor and heat treatment temperature. The supported nanoparticles may be considered to act as electrical switches either hindering or favouring the effective electron transport between the AC cores of neighbouring composite particles in contact under compression. Conductivity values as a rule were lower for the nanocomposites than for the raw AC, all of them falling in the range of semiconductor materials. With the increase in heat treatment temperature, the trend is toward the improvement of conductivity due to the increase in the crystallite size and, in some cases, to the formation of metals in the elemental state and even metal carbides. The patterns of variation of the electrical conductivity with pressure and mechanical work were slightly similar, thus suggesting the predominance of the pressure effects rather than the volume ones.

1. Introduction

In recent years, novel composites and hybrid materials based on metal and metal oxide nanoparticles (*i.e.*, particles having size in the range from 1 to 100 nm) supported on carbon materials have received a great deal of attention owing to their wide range of potential applications in heterogeneous catalysis, photocatalysis, gas and liquid adsorption, solid state gas sensors, electronics, energy storage devices, solar cells, and so on. Among the great variety of carbon materials, activated carbon (AC, henceforth) has been long selected as a support of metal-containing nanoparticles because of its excellent and unique properties, which have been the subject of several reviews and chapters in books.[1–5] Supported nanoparticles include not only metal oxides such as TiO_2, Fe_2O_3, ZnO, WO_3 and SnO_2, but also metal hydroxides and oxyhydroxides ($Ni(OH)_2$,[6,7] $Zn(OH)_2$,[8] and α-FeO(OH)[9,10]), and metals in the elemental state (Pt,[11] Au,[12] Ag,[13] Pd,[14] Ni,[15] Cu,[16] and so on). A comprehensive review on the preparation methods and applications of several metal oxides supported on AC has been recently reported elsewhere.[17]

In addition to the intrinsic properties of the single constituents, both the grain boundaries and the interfaces play a key role in the overall chemical and physical properties of the aforesaid carbon-based nanocomposites.[18] Among other factors, electrical conductivity is well known to largely determine the application and performance of these materials as electrode materials in energy storage devices, such as supercapacitors,[19,20] lithium ion batteries[21,22] and fuel cells.[23] On the other hand, several studies have found a correlation between the electrical conductivity of a wide range of metal oxides and their catalytic behaviour and/or

[a] *Department of Organic and Inorganic Chemistry, Faculty of Sciences, University of Extremadura, Avda. de Elvas s/n, E-06006 Badajoz, Spain. E-mail: adrianbogeat@unex.es; Fax: +34 924 271449; Tel: +34 924 289421*
[b] *Department of Mechanical, Energetic and Materials Engineering, University of Extremadura, Avda. de Elvas s/n, E-06006 Badajoz, Spain*

gas sensing properties.[24–29] Therefore, it becomes apparent that the measurement and comparison of the electrical conductivity of carbon-based composites containing nanoparticles of different metal oxides are key issues in order to assess many of their potential applications.

Nevertheless, in the case of granular, powder and porous materials such as AC–metal oxide nanocomposites, the determination of the electrical conductivity is rather complicated. According to the contact theory established by Mrozowski and Holm[30–32] more than sixty years ago, the electrical conductivity of a granular or powder carbon material depends not only on the interparticle separation distance,[33–38] but also on the mean particle size,[39] as well as on the chemical nature of the carbon surface. In this connection, the separation of the contribution of particle cores and surfaces to the bulk conductivity of several powder samples was methodically analyzed by Braun and Herger.[40]

Electron tunnelling, which entails the ability of electrons to jump across the gaps and voids between closely spaced grains and particles,[41] may be considered as the predominant electrical transport mechanism in granular and powder carbon materials. Consequently, the narrowing of gaps and the increase in contact between particles should lead to a significant increase in the bulk electrical conductivity of the sample. Since the pioneering studies conducted by Skaupy and Kantrowicz[42] on the electrical conductivity of compressed metal powders, many studies concerning the measurement of the conductivity of granular and powder materials under compression, in particular carbons,[30,36,43–47] have been reported.

The number of contacts established between neighbouring particles is of major relevance, as it determines the number of channels or paths available for the effective transport of electric current.[41] Several theoretical studies considering the particles as equal or roughly equal spheres in a random packing[48–51] have been performed in order to estimate the degree of contact between them during compaction. However, real situations are considerably more complicated, the mean number of contacts being almost impossible to determine since the particles may exhibit simultaneously a wide distribution of sizes and a strongly variable morphology,[44] which even may undergo changes during the compacting step.

In the present work, the electrical conductivity is studied under moderate compression (*i.e.*, from 99.5 to 756.0 kPa) for two series of AC–metal oxide nanocomposites, which were previously prepared by our research group from a commercial granular AC and six metal oxide (Al_2O_3, Fe_2O_3, SnO_2, TiO_2, WO_3 and ZnO) precursors by wet impregnation, oven-drying at 120 °C and subsequent heat treatment at two very different temperatures, 200 and 850 °C, in an inert atmosphere.[52,53] These temperatures were selected in order to investigate and compare the influence of the heating conditions on the electrical conductivity of the nanocomposites as a result of the phase composition changes undergone for each metal oxide precursor during the heat treatment stage. The influence of the applied pressure, volume change under compression, mechanical work, and density on the electrical conductivity is investigated for the resulting carbon-based hybrid materials. The obtained results are thoroughly discussed in terms of the content, chemical nature and crystallite size of the supported nanoparticles, and of the texture of the nanocomposites, and on the basis of Holm's contact theory.

2. Methodology

2.1. Materials

A granular AC purchased from Merck® (Darmstadt, Germany), of 1.5 mm average particle size (Cod. 1.02514.1000), as received without further treatment, was used as a support of a broadly varied series of metal oxides, including Al_2O_3, Fe_2O_3, SnO_2, TiO_2, WO_3 and ZnO. The selected metal oxide precursors were $Al(NO_3)_3{\cdot}9H_2O$, $Fe(NO_3)_3{\cdot}9H_2O$, $SnCl_2{\cdot}2H_2O$, $Na_2WO_4{\cdot}2H_2O$ and $Zn(NO_3)_2{\cdot}6H_2O$, all of them supplied by Panreac® (Barcelona, Spain) and being of reagent grade. As an exception to the rule, anatase powder from Aldrich® (Steinheim, Germany), less than 325 mesh average particle size, was used as a TiO_2 precursor.

2.2. Preparation of AC–metal oxide nanocomposites

The preparation of the AC–metal oxide nanocomposites was carried out following the methods previously described in detail by Barroso-Bogeat *et al.*,[52,53] which are briefly summarized in Table 1 together with the codes assigned to the resulting products. Accordingly, two series of hybrid materials were prepared depending on heating conditions, *i.e.* series 1 (200 °C, 2 h) and series 2 (850 °C, 2 h).

2.3. Characterization of AC–metal oxide nanocomposites

2.3.1. Ash content. The ash content of AC and hybrid materials was determined by incineration at 650 °C for about 12 h in air, using a muffle furnace (Selecta®). The soaking time at maximum heat treatment temperature was considered to be long enough to achieve the complete oxidation and conversion of the material fraction contained in each sample into gaseous products and residual ashes. The results were recently reported elsewhere,[53] and are collected in Table 2.

2.3.2. X-ray diffraction (XRD). As described before,[53] the crystalline phases present in each nanocomposite were investigated by powder XRD, using a D8 Bruker® Advance diffractometer

Table 1 Methods of preparation and sample codes for AC–metal oxide nanocomposites[a]

Series	Precursor	MHTT/°C	*t*/h	*A*	Code
Series 1	$Al(NO_3)_3{\cdot}9H_2O$	200	2	N_2	A200
	$Fe(NO_3)_3{\cdot}9H_2O$	200	2	N_2	F200
	$SnCl_2{\cdot}2H_2O$	200	2	N_2	S200
	TiO_2 (anatase)	200	2	N_2	T200
	$Na_2WO_4{\cdot}2H_2O$	200	2	N_2	W200
	$Zn(NO_3)_2{\cdot}6H_2O$	200	2	N_2	Z200
Series 2	$Al(NO_3)_3{\cdot}9H_2O$	850	2	N_2	A850
	$Fe(NO_3)_3{\cdot}9H_2O$	850	2	N_2	F850
	$SnCl_2{\cdot}2H_2O$	850	2	N_2	S850
	TiO_2 (anatase)	850	2	N_2	T850
	$Na_2WO_4{\cdot}2H_2O$	850	2	N_2	W850
	$Zn(NO_3)_2{\cdot}6H_2O$	850	2	N_2	Z850

[a] Abbreviations: MHTT, maximum heat treatment temperature; *t*, isothermal time at MHTT; *A*, atmosphere.

Table 2 Ash content, crystalline phases, and their weight fraction (W), mean crystallite size (D), density (ρ) and bulk electrical conductivity at room temperature (σ_{RT}) for the prepared AC–metal oxide nanocomposites

Sample	Ash content/wt%	Crystalline phase	W/%	D/nm	ρ/g cm^{-3}	σ_{RT}/S m^{-1}
A200	8.86	Alumina (Al_2O_3)	9.9	1.88	4.0–4.1	10^{-12} (ref. 58)
F200	13.55	Hematite (α-Fe_2O_3)	23.4	3.22	5.3	4.76×10^{-4} (ref. 59)
		Goethite (α-FeO(OH))	26.3	3.17	3.8	5×10^{-5} (ref. 60)
		Magnetite (Fe_3O_4)	9.6	6.19	5.2	2.25×10^{4} (ref. 61)
S200	27.21	Cassiterite (SnO_2)	16.0	4.05	6.9	1.9×10^{-4} (ref. 62)
		Romarchite (SnO)	5.0	5.07	5.5	5.40×10^{-4} (ref. 63)
T200	8.05	Anatase (TiO_2)	11.4	3.53	3.9	6.71×10^{-3} (ref. 64)
W200	9.93	Tungsten oxide (WO_3)	4.4	2.37	7.2	1.3×10^{-6}–7.5×10^{-6} (ref. 65 and 66)
		Tungstite ($WO_3 \cdot H_2O$)	1.4	3.05	5.5	6.7×10^{-2} (ref. 67)
Z200	9.45	Zinc oxide (ZnO)	0.9	20.80	5.6	4.8×10^{-8}–1.3×10^{-6} (ref. 68)
		Zinc hydroxide ($Zn(OH)_2$)	7.3	1.89	3.1	$<10^{-9}$ (ref. 8)
A850	5.68	Corundum (α-Al_2O_3)	11.0	2.06	4.0	
F850	14.66	Hematite (α-Fe_2O_3)	41.2	36.60	5.3	4.76×10^{-4} (ref. 59)
		Maghemite (γ-Fe_2O_3)	5.9	15.11	4.9	2.85×10^{-5} (ref. 69)
		Iron (Fe)	22.0		7.9	1.0×10^{7} (ref. 70)
S850	2.34	Cassiterite (SnO_2)	3.3	36.16	6.9	1.9×10^{-4} (ref. 62)
		Tin (Sn)	36.1	89.62	7.4[a]/5.8[b]	9.9×10^{6} (ref. 70)
T850	9.33	Anatase (TiO_2)	7.3	2.31	3.9	6.71×10^{-3} (ref. 64)
		Rutile (TiO_2)	7.1	1.86	4.3	$<10^{-7}$ (ref. 71)
W850	11.54	Tungsten (W)	9.0	48.36	19.3	1.9×10^{7} (ref. 70)
		Tungsten carbide ($W_6C_{2.54}$)	7.8	3.67		5.0×10^{4} (ref. 72)
Z850	6.18	Zinc oxide (ZnO)	0.6	69.38	5.6	4.8×10^{-8}–1.3×10^{-6} (ref. 68)

[a] White tin. [b] Grey tin.

working with Cu Kα radiation (λ = 1.5406 Å). The identification of the crystalline phases was accomplished by comparing peak positions and intensities with standard JCPDS files and with data previously reported in the literature. The mean crystallite size (D) was estimated for each of the crystalline phases in the nanocomposites by applying the Scherrer's equation[54,55] to their corresponding diffraction peaks:

$$D = \frac{K \cdot \lambda}{\beta \cdot \cos\theta} \quad (1)$$

where K is the so-called Scherrer's constant ($K = 0.94$[54]), λ is the wavelength of X-ray radiation, β denotes the full-width at half-maximum of the diffraction peak and θ is the characteristic Bragg angle of the crystalline phase.

The powder XRD patterns recorded for both series of nanocomposites are shown in Fig. 1. The crystalline phases supported on AC for each composite, as well as their corresponding weight fraction and mean crystallite size, have been reported in a previous work,[53] and are compiled in Table 2. The electrical conductivity of the phases covering the AC particles is very difficult to know, as it strongly depends on a number of factors such as the amorphous or polycrystalline nature of the phase, the presence of vacancies or dopant impurities, and so on.[56,57] Fortunately, the effects of the aforementioned factors usually alter only the conductivity values of the bulk phases by less than one order of magnitude, which can be found tabulated in specialised literature and have also been included in Table 2.

2.3.3. Textural data. The overall resistivity of granular and powder composites may be regarded as the sum of all the intraparticle and interparticle resistances. The intraparticle resistances are in turn determined by the intrinsic resistivity of the two single constituents (*i.e.*, supported nanoparticles and AC) and the resistance of the interface existing between them.[73] The resistance of each composite is largely a function of the matter-free space in the sample. This space comprises not only the interparticle voids, but also the porosity corresponding to the intraparticle voids. It is well known that in porous solids, such as activated carbons and carbon blacks, the microporosity (*i.e.*, the porosity region made up of pores of width smaller than $\sim$ 2 nm[74]) usually has the greatest contribution to the surface area. Herein, the specific surface area (S_{BET}) of AC and the prepared nanocomposites was estimated by applying the Brunauer, Emmet and Teller (BET) equation[75] to the N_2 adsorption isotherms measured at −196 °C in a semiautomatic adsorption equipment (Autosorb 1, Quantachrome®). The theoretical background for microporosity characterization was based on Dubinin's theory. Thus, the application of the Dubinin-Radushkevich (D-R) equation to the adsorption isotherms led to the values of the micropore volume (W_0).[76] The mesopore (V_{me}) and macropore (V_{ma}) volumes were derived from the mercury intrusion

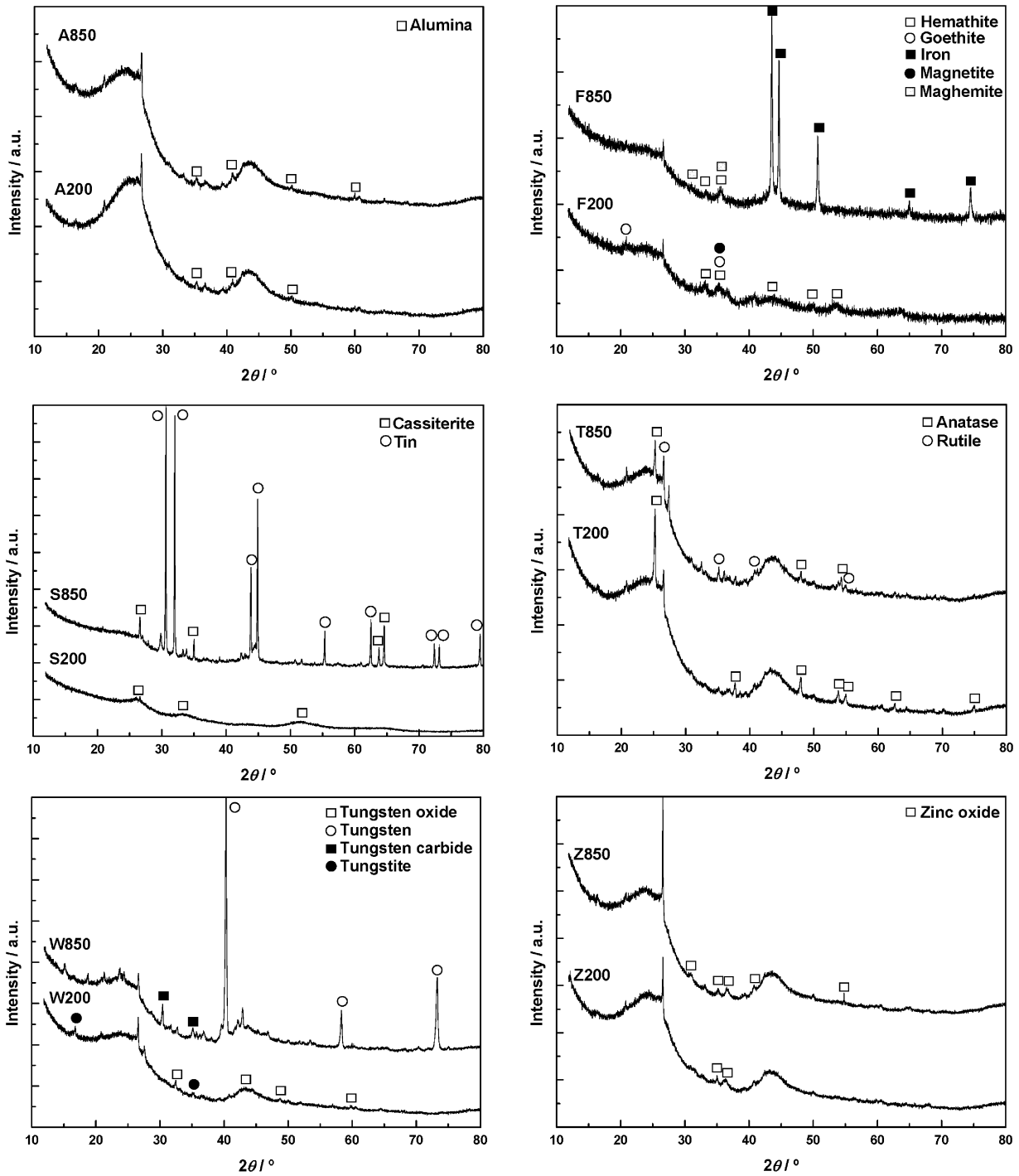

Fig. 1 Powder XRD patterns of nanocomposites of series 1 and 2.

curves obtained on a mercury porosimeter (PoreMaster-60, Quantachrome®). Finally, the total pore volume (V_T') was calculated from W_0, V_{me} and V_{ma}. These textural data for the raw AC and the prepared hybrid materials have been previously reported elsewhere,[52] and are listed in Table 3.

2.4. DC electrical conductivity measurements

Based on a standard procedure previously reported,[41,43,44,77] the DC electrical conductivity (σ) was measured at room temperature by the technique of impedance spectroscopy over the frequency range from 20 to 10^6 Hz at a voltage of 1 V, using the experimental set-up schematized in Fig. 2.[41] The masses of AC and nanocomposites used, after oven-drying at 110 °C overnight, were around 0.09 g, as seen in Table 3. Each accurately weighed sample was then poured into a hollow thick-walled PVC cylinder with an inner diameter of 0.8 cm, and compressed in air between two close-fitting brass plungers forming the electrodes, the lower one being fixed and the upper one movable. The compression

Table 3 Textural data and sample mass for AC and prepared nanocomposites

Series	Sample	S_{BET}/ $m^2\ g^{-1}$	W_0/ $cm^3\ g^{-1}$	V_{me}/ $cm^3\ g^{-1}$	V_{ma}/ $cm^3\ g^{-1}$	V_T'/ $cm^3\ g^{-1}$	m/g
	AC	711	0.36	0.15	0.21	0.72	0.0924
Series 1	A200	556	0.27	0.13	0.16	0.56	0.0908
	F200	618	0.29	0.13	0.14	0.56	0.0929
	S200	302	0.15	0.08	0.13	0.36	0.0916
	T200	776	0.35	0.13	0.19	0.67	0.0922
	W200	646	0.32	0.15	0.17	0.64	0.0963
	Z200	651	0.31	0.18	0.20	0.69	0.0941
Series 2	A850	759	0.34	0.14	0.19	0.67	0.0948
	F850	694	0.31	0.17	0.18	0.66	0.0974
	S850	680	0.33	0.16	0.18	0.67	0.0910
	T850	847	0.37	0.14	0.20	0.71	0.0912
	W850	741	0.35	0.15	0.20	0.71	0.0903
	Z850	834	0.32	0.15	0.18	0.65	0.0935

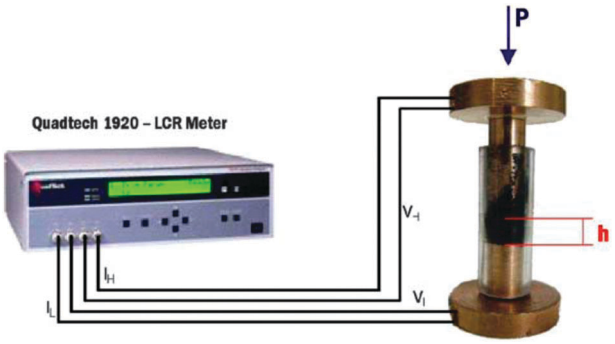

Fig. 2 Experimental assembly for measuring the electrical conductivity of granular and powdered materials under moderate compression.

pressures ranged from 99.5 to 756.0 kPa, which were achieved by applying different loads between 5 and 38 N on the upper piston by a universal testing machine (Shimadzu®), with a precision of 1 μm in the compression plate movement. In this regard, it should be noted that this range of applied pressures was not very wide; the lowest pressure was enough to get a good electrical contact between the sample particles and the plungers, whereas the highest one was too low to cause the crushing and breaking of the grains. Consequently, the increase in the volume fraction of particles due to their spatial rearrangement is expected to be the only effect of the compaction. The very small changes produced in the height of the sample bed as a consequence of the compression were obtained from the corresponding stress–strain curve. The DC electrical resistance was measured by the four-probe method[43,45] using a digital multimeter (model 34411A, Agilent®). After a series of preliminary tests, 5 min were allowed prior to measuring the resistance in order to avoid any transient effect of sample relaxation. The four probes, *i.e.* I_L, I_H, V_L, and V_H, were connected to the electrodes as illustrated in Fig. 2. Conduction was considered to be ohmic in nature, so the electrical conductivity was estimated using the following expression:[30]

$$\sigma = \frac{h}{R \cdot A} \quad (2)$$

where R is the electrical resistance in Ω, A the area of the plunger surface in m^2, and h denotes the distance between the two plungers in the compression chamber, or the height of the sample bed, in m. The resistance of the plungers was verified and found to be at around 0.050 Ω, much lower than those of the samples under study. The electrical conductivity (σ), volume (V) and density (ρ) were determined for each sample and at each applied pressure (P). V was roughly estimated by considering the compressed sample as a cylinder having a base of surface area A and height h:

$$V = A \cdot h \quad (3)$$

while ρ was given by:

$$\rho = \frac{m}{V} = \frac{m}{A \cdot h} \quad (4)$$

3. Results and discussion

3.1. Change in the sample volume under compression

Fig. 3(a) and (b) show the variation of the sample volume (V) with applied pressure (P) for nanocomposites of series 1 and 2, respectively. The plot for the raw AC has also been included in the above figures for comparison purposes. V, as determined, must be regarded as a very rough estimation of the bulk volume, since the granular morphology of the samples leads to a loose packing of the grains with voids between them, and not even at the highest P value it can be ensured that the total void space has been entirely excluded. Consequently, this volume is higher than the bulk volume (*i.e.*, that measured by mercury porosimetry[78,79]), and decreases with increasing pressure to approach the latter. It is seen first that for most nanocomposites the total reduction in V with increasing P is relatively small, less than 7%, and lower than that observed for AC (10.4%), being only significant for samples Z200 and Z850 (11.0 and 9.7%, respectively). As a rule, the decrease in V is more important at low P values, below ≈100 kPa, while at higher pressures the variation is nearly linear and negligible. Moreover, V is rather similar for AC and most composites over the entire P range, and it varies in the order: S200 ≪ A200 < F200 ≈ T200 ≈ Z200 < AC < W200 for samples of series 1, and by: A850 < S850 < W850 < Z850 ≈ T850 ≈ AC ≪ F850 for those of series 2. As seen in Table 3, the hybrid materials prepared at 200 °C possess a very different degree of development of their surface area, with S_{BET} values widely ranging from 302 $m^2\ g^{-1}$ for S200 to 776 $m^2\ g^{-1}$ for T200, whereas the specific surface area is more homogeneous for nanocomposites prepared at 850 °C, as it varies in the narrow range between 680 $m^2\ g^{-1}$ for S850 and 847 $m^2\ g^{-1}$ for T850. Therefore, the extent of surface area of the composites should not be identified as the main factor in the magnitude of change in V produced by compression. Neither is the microporosity of the samples, since it is well known that for porous solids the surface area is largely concentrated in the micropores.[41] Conversely, the mesoporosity and the macroporosity of the hybrid materials are likely to play a more important role than the above factors, especially for composites of series 1.

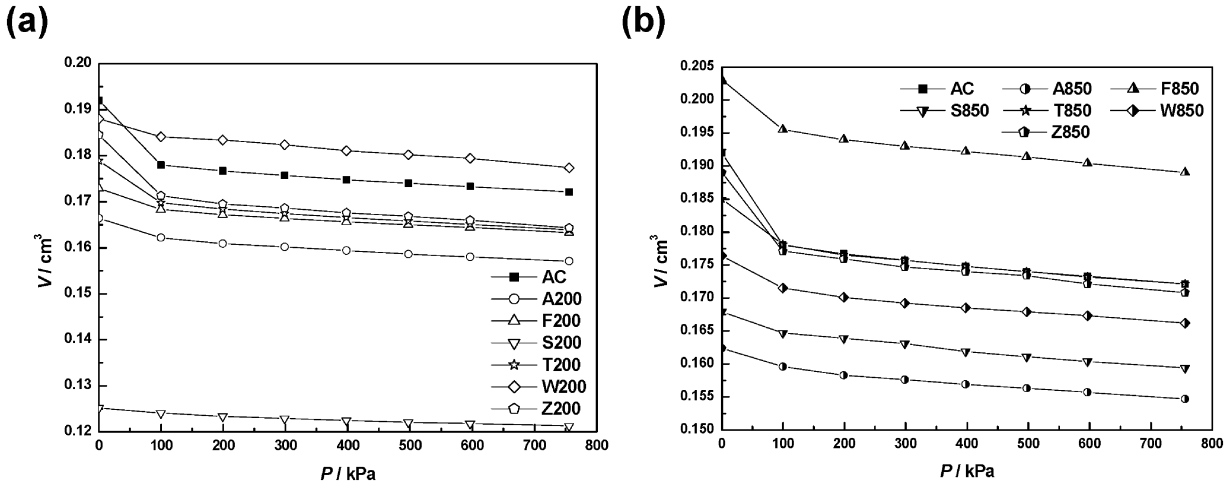

Fig. 3 Sample volume *versus* applied pressure for nanocomposites of (a) series 1 and (b) series 2.

Indeed, from Table 3 one observes that V_{me}, V_{ma} and V_T' are markedly lower for S200 than for AC and the rest of the samples prepared at the same temperature, and the latter is higher as follows: S200 $\ll$ A200 $\approx$ F200 $<$ W200 $<$ T200 $<$ Z200 $<$ AC, which is in good agreement with the sequence obtained for the variation of V with P. Nevertheless, such a correlation cannot be established for composites of series 2, as V_T' increases in the following order: Z850 $<$ F850 $<$ A850 $\approx$ S850 $<$ T850 $\approx$ W850 $<$ AC. As a rule, the slight differences in V with increasing P for AC and most of the nanocomposites, irrespective of their heat treatment temperature, may be explained by taking into account that the V_T' values fall within a very narrow range from 0.56 $cm^3\ g^{-1}$ for A200 to 0.72 $cm^3\ g^{-1}$ for the carbon support. The great contribution of V_T' to V comes from the fact that the former cannot be completely excluded from the latter without crushing and breaking the grains, which usually requires compression pressures much higher than those applied in the present work. In this regard, it is worth noting that for AC and most composites V_T' accounts for more than a third of V at any P value. Thus, for example, V_T' is about 39% of V for A850 without compression, a value which rises up to 41% at P = 756.0 kPa.

3.2. Variation of ρ with P

The density is an intrinsic property of each hybrid material. The variation of ρ with P for nanocomposites of series 1 and 2 is depicted in Fig. 4(a) and (b), respectively, together with the curve for AC. Similarly to the sample volume, the density, as estimated in the present work, must be considered as a very rough estimate of the bulk density. Such density is lower than the apparent density, *i.e.* that measured in a typical mercury porosimetry experiment,[78,79] and increases with the applied pressure to approach the latter. As can be seen from the above figures, both AC and all the composites show a quite similar densification-pressure behaviour, namely a linear dependence of density on the applied pressure at $P > 100$ kPa. Analogous densification behaviour has been recently reported by Marinho *et al.*[46] for a variety of carbon materials, including graphene, multiwalled carbon nanotubes, carbon black and graphite powder, which they interpreted as follows. After pouring the

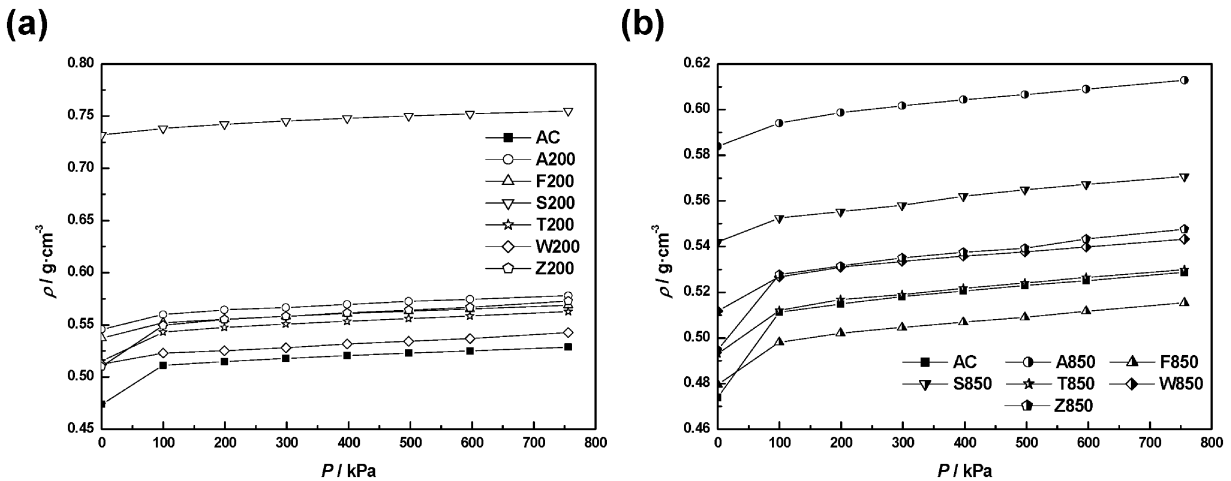

Fig. 4 Density *versus* applied pressure for nanocomposites of (a) series 1 and (b) series 2.

sample into the hollow plastic cylinder, a loose packing with large voids between the particles and grains is obtained. Under moderate compression (*i.e.*, within the range of pressures applied in this work), densification is mainly attributable to the rearrangement of grains controlled by the interparticle friction and, thereby, no significant changes in the internal porous structure of the single particles are expected. Moreover, for most nanocomposites the overall increase in ρ with increasing P is very low, and more relevant at $P < 100$ kPa, in line with that stated above for the variation of V. At higher P values, the variation is linear and the corresponding fitted lines have an almost identical slope for AC and all the hybrid materials. Over the entire P range, the order of the variation of ρ is AC < W200 < T200 < F200 ≈ Z200 < A200 < S200 for samples heated at 200 °C, and F850 < AC ≈ T850 < W850 ≈ Z850 < S850 < A850 for those prepared at 850 °C. If one assumes that the density of the supported nanoparticles (see Table 2; here we have considered such density to be roughly equal to the bulk density, although in the case of nanoparticles the density has been recently reported to be dependent on the particle size[80]) is as a rule much higher than that of the raw AC (2.0 g cm^{-3}, measured by helium pycnometry[52]), then the density of the nanocomposites should increase with their ash content, since the greater the latter, the larger the amount of the aforesaid nanoparticles supported on AC. As seen in Table 2, the ash content increases in the following order: T200 < A200 < Z200 < W200 < F200 < S200 for samples of series 1, and by: S850 < A850 < Z850 < T850 < W850 < F850 for those of series 2. Strikingly, a correlation of density with the ash content is not found; indeed, for composites heated at 850 °C the density behaviour is nearly the opposite to the expected one according to the ash content values. The differences between both variation sequences for density and ash content are likely connected with the density of the supported inorganic phases, which is a very important factor as it widely ranges between 3.1 g cm^{-3} for $Zn(OH)_2$ and 19.3 g cm^{-3} for metallic W.

Finally, it is worth mentioning that the similar behaviour of V and ρ under compaction for AC and all nanocomposites, regardless of their metal oxide precursor and heat treatment temperature, clearly suggests that the mechanical properties of the latter are mainly determined by the carbon matrix.

3.3. Study of electrical conductivity

The values of σ measured for the AC support and the prepared hybrid materials at two P values, P = 99.5 kPa (σ_1) and P = 756.0 kPa (σ_2), are collected in Table 4. One notes that all the samples show values of σ_1 and σ_2 falling in the range of conductivity of typical semiconductor materials, *i.e.* from 10^{-8} to 10^5 S m^{-1}.[81] This fact should not be surprising, since several previous studies have pointed out the semiconductor behaviour for a number of carbon materials, such as activated carbons prepared from different lignocellulosic precursors by both chemical and physical activation methods,[82–85] amorphous carbons[86–89] and carbon-based composites.[18] Furthermore, the nanoparticles detected by powder XRD in the prepared carbon-based hybrid materials are mostly metal oxides (Al_2O_3, Fe_2O_3, SnO, SnO_2, TiO_2, WO_3 and ZnO), which are well known to be wide band gap semiconductors.[17] Therefore, the presence of these oxides must decisively contribute to the semiconductor properties exhibited by the hybrid materials. In addition, the values of σ_1 and σ_2 are as a rule markedly lower for the nanocomposites than for the pristine AC, except for the sample W850. The greatest electrical conductivity for this composite may be related to the presence of nanoparticles of elemental tungsten and the non-stoichiometric tungsten carbide $W_6C_{2.54}$ as unique supported metal phases, whose intrinsic conductivity values at room temperature (see Table 2) are noticeably higher than for other metal phases. Table 4 also lists the percentage of increase in electrical conductivity (PIEC), which is defined as follows:

Table 4 Electrical conductivity of AC and prepared nanocomposites at two pressure values

Series	Sample	σ_1/S m^{-1} P = 100 kPa	σ_2/S m^{-1} P = 756 kPa	PIEC[a]
	AC	57.3	194.1	239
Series 1	A200	25.1	103.7	314
	F200	7.8	40.0	415
	S200	23.3	162.3	597
	T200	52.2	172.0	229
	W200	38.5	161.1	319
	Z200	35.8	149.1	317
Series 2	A850	40.9	150.8	269
	F850	36.9	131.5	256
	S850	41.9	173.4	314
	T850	44.4	172.5	288
	W850	63.8	209.5	229
	Z850	48.3	157.2	226

[a] Percentage of increase in electrical conductivity.

$$\mathrm{PIEC} = \frac{(\sigma_2 - \sigma_1)}{\sigma_1} \times 100 \quad (5)$$

3.3.1. Variation of σ with P. The plots of σ against P for the hybrid materials prepared by heating at 200 and 850 °C are shown in Fig. 5(a) and (b), respectively. As expected, σ increases with P for all samples, and a good linear relationship is also observed between them, irrespective of the heat treatment temperature. As stated above, the electrical conductivity strongly depends on the number of effective electrical contacts which are established between the sample particles, since this determines the number of channels or paths available for the transport of electric current. Under compression, the neighbouring particles are forced to approach each other, readily increasing the number of electrical contacts and hence the conductivity.[30,41] A few previous studies have revealed that the electrical conduction under compression in different granular and powder carbon materials,[30,45,47] especially carbon blacks,[41,90] is usually favoured by a smaller sample volume. Nevertheless, such an effect of sample volume on electrical conductivity is not observed in the case of these nanocomposites, since over a wide P range σ varies in the order: AC > T200 > S200 ≈ W200 > Z200 > A200 > F200 for 200 °C samples, and by: W850 > AC > T850 ≈ S850 > Z850 > A850 > F850 for 850 °C samples. Neither a correlation between the above sequences and the total variation in V under compression is found.

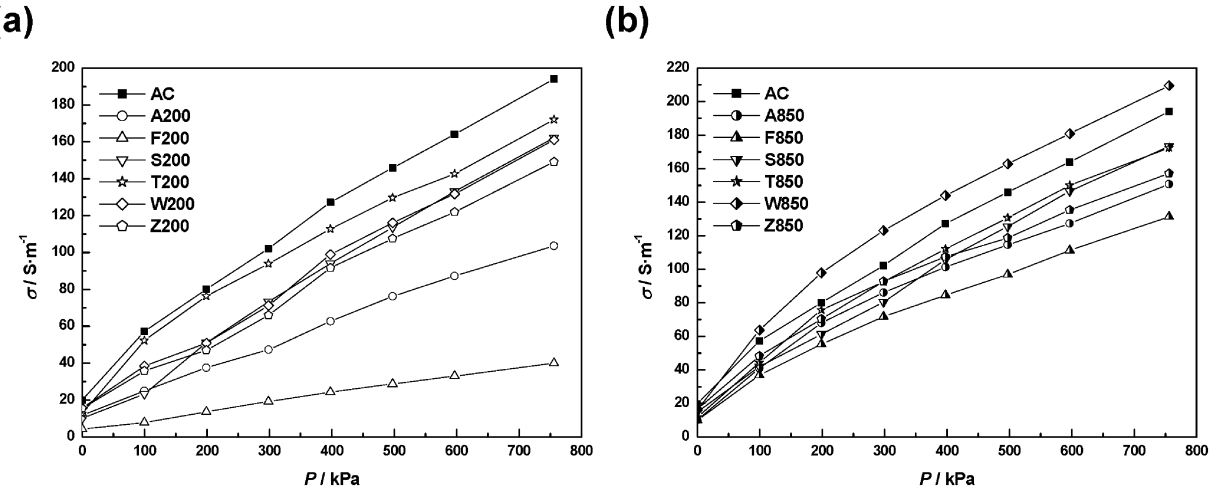

Fig. 5 Electrical conductivity *versus* applied pressure for nanocomposites of (a) series 1 and (b) series 2.

As shown in Table 3 and previously discussed in detail elsewhere,[52] the preparation of AC–metal oxide nanocomposites by wet impregnation of AC with the metal oxide precursor, oven-drying at 120 °C, and subsequent heat treatment at 200 °C in an inert atmosphere, leads to a decrease in the three porosity regions, *i.e.* micro-, meso- and macroporosity, for the resulting products as compared to the raw AC. Conversely, by heat treatment at 850 °C porosity develops for all hybrid materials, the increase being more pronounced in the region of micropores. However, the micropore volume (W_0) as a rule is significantly lower for these composites than for the carbon support. In brief, both heat treatments at 200 and 850 °C cause a reduction of porosity in the three regions of pore sizes, which is less marked for the nanocomposites prepared at the highest temperature. Unlike the behaviour observed for other porous carbon materials, such a reduction in porosity, and hence in the total intraparticle void space (*i.e.*, V_T'), does not result in an improvement of the electrical conductivity of AC, since most hybrid materials exhibit σ values lower than the carbon support over the entire P range (see Fig. 5(a) and (b)). As the only exception to this rule, the conductivity is noticeably higher for W850. Therefore, it becomes apparent that the porosity of AC is partially filled and blocked by a variety of nanoparticles having a much lower conductivity than the carbon support itself. As far as the composites of series 1 are concerned, such nanoparticles are essentially metal oxides, whose electrical conductivity values at room temperature (see Table 2) are generally several orders of magnitude lower than that measured for the raw AC (σ_{RT} = 19.9 S m^{-1}). In this regard, the conductivity of these hybrid materials should decrease with increasing the content of nanoparticles and, thereby, with the ash content (for its variation, see Section 3.2). However, this correlation is not observed and, similarly to that stated above for the variation of ρ with P, the reason may be attributable to the very different intrinsic conductivity values of the supported nanoparticles. Thus, the relatively low σ values registered for A200 are explained by the insulating character of the supported alumina,[58,91] even though such a composite should theoretically exhibit higher conductivity due to its low ash content. Likewise, the highest ash content for S200 should give the poorest σ values for this hybrid material. Nevertheless, from Fig. 5(a) it is seen that the σ–P plot for S200 is situated significantly above than those of F200 and A200. This fact seems to be related to the much greater electrical conductivity of cassiterite (SnO_2) and romarchite (SnO) as compared to hematite (α-Fe_2O_3) and goethite (α-FeO(OH)), and with alumina (Al_2O_3), which are the predominant phases detected in S200, F200 and A200 (see Table 2).

From Fig. 5 and data in Table 4 it is evident that the increase of heat treatment temperature from 200 to 850 °C as a rule leads to an improvement of conductivity for the resulting nanocomposites. This behaviour may be explained on the basis of composition and structural changes in the carbon support and the supported nanoparticles originated by the heat treatment at 850 °C and with influence on electrical conductivity of the hybrid materials, as seen below. First, as previously discussed elsewhere,[52,53] carbothermic reductions of metal oxides occur during heating at a temperature as high as 850 °C. As shown in Table 2, these reactions give rise to the formation of nanoparticles of elemental metals, mainly Fe, Sn and W, and even of metal carbides, such as $W_6C_{2.54}$. In this connection, it should be noted that a great variety of iron species, including several iron oxides (FeO,[92] γ-Fe_2O_3,[93] and Fe_3O_4[94]) and carbides (Fe_3C[92] and Fe_4C[92]), as well as elemental iron,[93] have been detected in carbon–iron composites prepared under similar heating conditions. However, only α-Fe_2O_3, elemental iron and a small amount of γ-Fe_2O_3 are detected in sample F850, these results being in good agreement with those obtained in previous studies of preparation of AC–iron oxide composites.[95–98] The intrinsic conductivity of the aforesaid metals and metal carbides is many orders of magnitude higher than for the corresponding metal oxides and, obviously, their presence in the nanocomposites causes a significant enhancement in electrical conductivity. Second, regardless of the metal oxide precursor, the heat treatment at 850 °C usually results in the development of crystallinity and in an increase of the crystallite size for the supported nanoparticles,[53] which also contribute to the better conductivity exhibited by these composites. In this regard,

a number of previous studies dealing with the dependence of electrical properties on crystallite size for nanoparticles of a wide variety of metal oxides[99–103] and metals[104] have shown that the larger the crystallite size, the smaller the width of the insulating grain boundary and, thereby, the greater the electrical conductivity. Furthermore, from Table 4 one can infer that the presence of zero-valent metal nanoparticles appears to be a stronger factor than the increase of the crystallite size on the improvement of conductivity of the hybrid materials with increasing heat treatment temperature. Indeed, the increase in conductivity is markedly greater for sample F850 and also, though less, for S850 and W850, which are those containing metals in the elemental state, whereas such an increase is less pronounced for the rest of the nanocomposites. As an exception to the rule, conductivity only decreases slightly for T850, likely due to the smaller crystallite size. It is worth noting that rutile originates from anatase by means of a phase transition occurring in the temperature range from 600 to 700 °C for TiO_2–carbon hybrid catalysts.[105] As previously reported by Czanderna *et al.*,[106] this phase transition occurs extremely fast at temperatures above 730 °C. Therefore, a complete transformation of the initial pure anatase into rutile would be expected in the case of T850 due to the heat treatment at 850 °C for 2 h. Nevertheless, the powder XRD pattern of T850 clearly reveals that only half of the anatase is converted into rutile after such heat treatment. These results are in good agreement with those previously obtained in the preparation of AC–TiO_2 composites by the sol–gel method.[107,108] The effect of the AC matrix on the TiO_2 phase transformation has been thoroughly investigated by Y. Li *et al.*[108] They found that the temperature of the anatase to rutile phase transition in AC–TiO_2 composites is higher than that observed in pure anatase powders. This behaviour was attributed to the high surface area AC matrix, which alters the phase transition due to its large interfacial energy, thus resulting in anti-calcination effects for the AC matrix. In addition, the small amounts of SiO_2 in the AC support (around 1.2 wt%), and coming from the inorganic matter present in the AC precursor, have also been suggested to constrain the anatase to rutile transformation, probably as a result of the formation of Ti–O–Si bonds during the heat treatment, which are much more difficult to recombine with other Ti–O bonds, thus retarding the phase transition.[109]

The conductivity σ is markedly influenced by the applied pressure (see Fig. 5(a) and (b) again), especially for composites of series 1. At low P values, up to $\approx$100 kPa, σ is quite similar in value for all the composites prepared at 850 °C and slightly lower than for AC, except for W850, while the differences in σ are more significant in the case of the 200 °C samples. At higher P, the greatest increase in σ occurs for T200, W200 and S200, and for W850, T850 and S850. The PIEC values collected in Table 4 clearly show that the effect of increasing P on σ is very strong for AC and both series of hybrid materials, being somewhat weaker for those prepared at higher temperature. Such values range between 229 for T200 and 597 for S200, and from 226 for Z850 to 314 for S850. The variation sequences follow the order S200 > F200 > W200 $\approx$ Z200 $\approx$ A200 > AC > T200 for series 1, and S850 > T850 > A850 > F850 > AC > W850 $\approx$ Z850 in the case of series 2. The plots of σ divided by ρ against P for AC and the prepared nanocomposites are fairly similar to those of σ *versus* P in Fig. 5(a) and (b). Therefore, they have been omitted for the sake of brevity.

On the other hand, based on an increase in the contact area between the particles and grains as a result of compression, Holm proposed the following exponential dependence of σ on P for powder and particulate materials:[31,32]

$$\sigma = \alpha \cdot P^{\beta} \quad (6)$$

where both α and β are constants whose values depend only on the material properties. A value of β of about 0.5 has been associated with the elastic contact between the particles, whereas for the plastic contact β has been estimated to be around 0.33. The above equation was used to fit the experimental data shown in Fig. 5(a) and (b), and the results are gathered in Table 5. It is seen that irrespective of the metal oxide precursor and the heat treatment temperature, the data as a rule fit well to Holm's equation, R^2 values being above 0.99. The β values for AC and all composites are much closer to 0.5 than to 0.33, especially for samples prepared at 850 °C, thus suggesting a nearly elastic contact between the particles rather than plastic deformation. The latter assertion is also corroborated from the corresponding strain–stress curves, which exhibit the linear relationship typical of the elastic behaviour over the entire range of applied pressures (these plots have been omitted for the sake of brevity). Moreover, for hybrid materials of series 1, it also becomes apparent that the deviation from the elastic deformation behaviour is greater for those samples with higher ash content and, presumably, with a larger amount of supported nanoparticles. In fact, the highest β value is obtained for S200, having an ash content of 27.21%. Nevertheless, a similar correlation has not been observed in the case of the composites prepared at 850 °C.

3.3.2. Variation of σ with volume. Similarly to density, the sample volume under compression may also be regarded as another intrinsic property of each hybrid material. Fig. 6(a) and (b) reveal that similar σ values are achieved with extremely different sample volumes and, in the same way, identical sample volumes also lead to very different σ values. For example, in the case of series 1, a conductivity of 80 S m^{-1} is obtained with a sample volume of $\approx$0.123 cm^3 for S200, 0.158 cm^3 for A200 and 0.182 cm^3 for W200, being $\approx$0.177 cm^3 for AC. Concerning series 2, the above conductivity value requires a sample volume of $\approx$0.158 cm^3 for A850, 0.175 cm^3 for Z850 and 0.192 cm^3 for F850. Therefore, it is evident that the range of sample volumes

Table 5 Fit parameters for the Holm equation

Sample	α	β	R^2	Sample	α	β	R^2
AC	3.32	0.61	0.9957	AC	3.32	0.61	0.9957
A200	0.88	0.71	0.9900	A850	2.36	0.63	0.9967
F200	0.19	0.81	0.9997	F850	2.08	0.62	0.9985
S200	0.32	0.95	0.9952	S850	1.45	0.72	0.9910
T200	3.56	0.58	0.9969	T850	2.18	0.66	0.9970
W200	0.51	0.87	0.9951	W850	4.48	0.58	0.9994
Z200	0.47	0.87	0.9950	Z850	3.35	0.58	0.9982

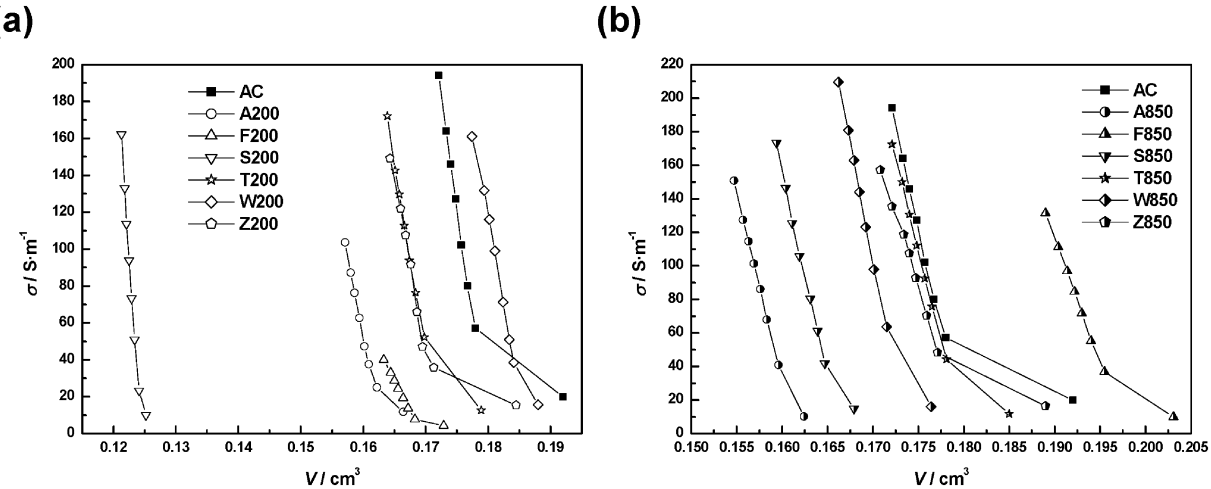

Fig. 6 Electrical conductivity *versus* volume for nanocomposites of (a) series 1 and (b) series 2.

needed for reaching a given conductivity value is much broader for composites prepared at 200 °C. Despite the foregoing, it is also seen that the sensitivity of σ to the volume change is as a rule quite similar for AC and all the twelve nanocomposites, given that their corresponding σ–V curves are rather similarly shaped and almost parallel. Furthermore, one observes in Fig. 6(a) and (b) that the evolution of σ with decreasing V exhibits a good linear relationship for all the samples at $P >$ 100 kPa. Since for most hybrid materials the volume change is greater at P values lower than the above, the results indicate that only after the samples have undergone an initial volume reduction is further compression more effective in increasing their electrical conductivity. After such a reduction, small changes in the sample volume as a result of increasing pressure lead to a great enhancement in σ.

Fig. 5 and 6 show that the relative magnitude of σ as a rule depends on whether the plot is depicted against P or V. In the case of T200 and Z200, as an example, σ is nearly identical over a wide V range, but significantly higher for T200 over almost the entire P range. For T850 and W850, σ is markedly higher for the latter over the entire P range, whereas the opposite applies over a wide V range.

3.3.3. Variation of σ with mechanical work. The plot of σ against the mechanical work (MW, henceforth) allows analyzing together the opposite effects of P and V on σ. MW has been estimated for each sample using the following equation:[110]

$$\mathrm{MW} = \sum_{j=1}^{i} p_j \cdot A \cdot \left(h_{j-1} - h_j\right) \qquad (7)$$

where A is the surface area of the piston and p_j denotes the pressure required to cause a change of $(h_{j-1} - h_j)$ in the height of the sample bed. Thus, the value of MW is identified with the resistance of a given sample to be reduced in volume by compression. The above equation is fully applicable in the case of a homogeneous medium. Nevertheless, its applicability for non-homogeneous media, such as AC and the hybrid materials studied in the present work, is very questionable as the significant effects of orientation of the grains, and of pressure inhomogeneities in the sample bed, are obviated.[41] As reported by Celzard *et al.*,[44] such effects depend on several factors, especially the kind of carbonaceous material (*e.g.* activated carbon, powder graphite or carbon black, among others), the bed height and the applied pressure. In the present study, for obtaining comparable results, only a narrow range of initial heights of the sample column between 2.5 and 4.0 mm was used, while the pressure range was the same for AC and all twelve nanocomposites. The evolution of σ with MW is illustrated in Fig. 7(a) and (b).

As can be seen, for each sample, the σ–MW curve is faintly similar to the σ–P plot (Fig. 5(a) and (b)) but it does not bear any resemblance to the σ–V plot (Fig. 6(a) and (b)), thus suggesting that the applied pressure rather than the sample volume is the predominant factor responsible for the variation of σ with MW. Such behaviour is related to the fact that, as previously shown in Fig. 3(a) and (b), a large increase in P is usually required to produce a relatively small reduction in the sample volume. As a rule, for AC and both series of composites, σ sharply increases until a certain value of MW is reached and, then, the rise flattens out. This occurs in the narrow range between 4×10^{-4} and 5×10^{-4} J for AC and most composites. In addition, for a given metal oxide precursor, the increase in heat treatment temperature from 200 to 850 °C does not significantly modify the shape of the σ–MW curves for the resulting hybrid materials. However, it must be pointed out that the distribution of the σ–MW curves in Fig. 7(a) and (b) is extremely different from that obtained for the σ–P plots in Fig. 5(a) and (b), where some of the curves, especially those for composites of series 2, lie very close to each other. These results clearly indicate that σ is more sensitive to the increase in MW than in P and, therefore, the AC and the prepared hybrid materials are better discriminated by using the extrinsic factor MW. Indeed, for samples S200 and W200, a conductivity of $\approx$70 S m^{-1} is achieved with a $P \approx$ 300 kPa, whereas MW values of 1.5×10^{-4} and 3.0×10^{-4} J, respectively, must be applied to reach the same conductivity value. In the same way, under a $P \approx$ 756 kPa nanocomposites

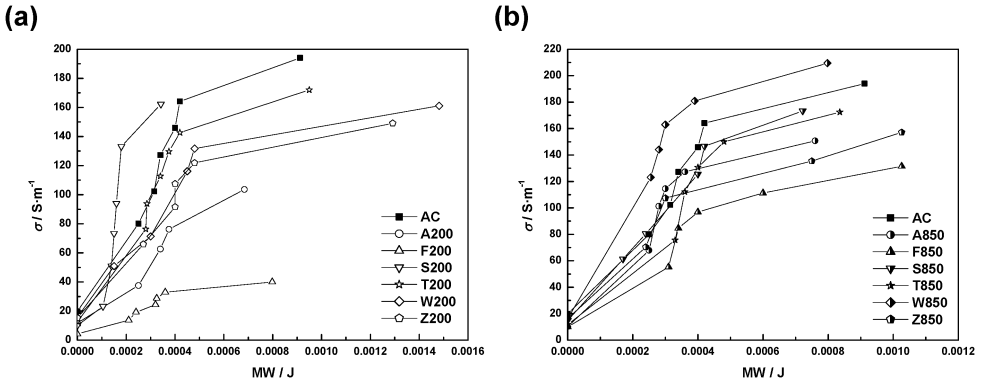

Fig. 7 Electrical conductivity *versus* mechanical work for nanocomposites of (a) series 1 and (b) series 2.

A850 and Z850 exhibit a conductivity of $\approx$155 S m^{-1}, which requires MW values of 7.6×10^{-4} and 1.0×10^{-3} J, respectively.

3.3.4. Variation of σ with ρ. The variation of σ with ρ for composites of series 1 and 2 is depicted in Fig. 8(a) and (b), respectively. As expected, for each hybrid material, the σ–ρ plot closely resembles the σ–V plot. Unlike the behaviour observed for other carbon materials, mainly carbon blacks,[41,110] the total variation in σ with increasing ρ of the samples by compression appears not to be dependent on the density of the nanocomposites. In the case of samples prepared at 200 °C, the increase in σ is roughly as follows: AC > T200 > S200 $\approx$ W200 > Z200 > A200 >> F200, while for those prepared at 850 °C it varies in the order: W850 > AC > S850 $\approx$ T850 > A850 $\approx$ Z850 > F850. In both cases, a clear correlation between the variation sequences of σ with ρ and ρ with P is not found. Furthermore, σ increases steeply and almost linearly with ρ at P values above *ca.* 100 kPa, the slope of the fitted lines being quite comparable for AC and all the hybrid materials. In this regard, an analogous linear relationship between σ and ρ has also been reported elsewhere[46] for compacts of several carbon materials, including graphene, multiwalled carbon nanotubes and graphite powder. This variation of σ with increasing ρ of the samples may be explained as follows. The electrical conductivity is strongly determined by the number of effective electrical contacts that are established between neighbouring particles and grains of the samples. On this basis, one may conclude that for each sample the number of electrical contacts, and thereby the conductivity, should be primarily a function of its density, among other factors, since the greater the density, the closer the particles and the less the void space between them, which strongly contributes to the bulk electrical resistance of the material. Under compression, the neighbouring particles of the sample are forced to approach each other, thus increasing both the density and the number of electrical contacts. As shown in Fig. 8(a) and (b), a small increase in the density of AC and the hybrid materials leads to a large enhancement in electrical conduction, which clearly reveals the loose packing of the sample particles just prior to starting the compaction experiments.

As previously shown for other carbon materials,[41,44,111] the morphology of the samples may also play a major role in their electrical conductivity. Nevertheless, the influence of this factor on the conductivity of the prepared hybrid materials has been omitted in the present work, since the particle size distribution is almost identical for AC and all composites with an average particle size of $\approx$1.5 mm.

In order to simplify and address the problem of the electrical conduction in the prepared nanocomposites under moderate compression, they have been modelled as particulate materials consisting of AC grains partially coated by nanoparticles of metal oxides, which may also be accompanied by hydroxides, oxyhydroxides, metals in the elemental state and even carbides, depending both on the metal oxide precursor and the heat

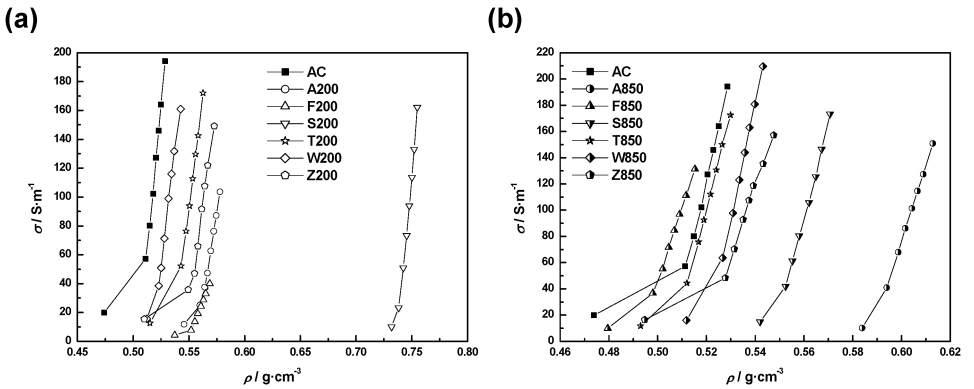

Fig. 8 Electrical conductivity *versus* density for nanocomposites of (a) series 1 and (b) series 2.

treatment temperature (see Table 2). This simplified model is in line with the mean crystallite size estimated for the various supported metal phases (see Table 2 again), which ranges from 1.88 nm for Al_2O_3 in A200 to 20.80 nm for ZnO in Z200, and between 1.86 nm for TiO_2-rutile in T850 and 89.62 nm for Sn in S850. A few previous studies dealing with the electrical behaviour of lightly compacted metal powders from both theoretical and experimental standpoints[56,112–115] have proved that the very thin films coating the metallic powder particles do not affect the mechanical properties, but substantially alter the electrical properties of the powder mass, particularly at the early stages of the compression experiment. Such an assertion seems to be fully valid for the prepared carbon-based hybrid materials since, as stated above, their mechanical properties (*i.e.*, densification and deformation behaviours) are quite similar to those of the raw AC, while their electrical conductivity is largely controlled by the different nanoparticles supported on the AC surface. However, several metal phases can be found together at different proportions in a single nanocomposite (as an illustrative example, consider the case of the sample F200), which usually makes a very difficult task to accurately know the actual electrical conductivity of the nanoparticles covering the AC grains.

The electrical contacts will be more effective, and then will allow electron transport easily, when they are established between points of carbon surfaces belonging to neighbouring composite particles, as one infers from the greatest conductivity values measured for the pristine AC. The metal oxide, hydroxide and oxyhydroxide nanoparticles in the prepared hybrid materials act as insulating thin layers due to their much lower electrical conductivity values as compared to the carbon support. Therefore, the contacts between close composite particles involving the aforesaid insulating films will be less effective as paths for the electron transport, thus increasing the contact resistance and decreasing the bulk electrical conductivity of the hybrid material. Conversely, highly conductive nanoparticles of metals in the elemental state and metal carbides detected in composites F850, S850 and W850 are likely to favour the electrical current flow under compression, as long as they are located in the small contact area between two sample particles. In this connection, it should be noted that for the pair of composites F850 and S850 elemental iron and tin are accompanied by their corresponding oxides Fe_2O_3 and SnO_2. Of both opposite effects of metal oxides and elemental metals on the electrical properties of the prepared hybrid materials, the former appears to be stronger so that the bulk conductivity of the above samples is still noticeably lower than for AC. In contrast, for W850 only metallic tungsten and tungsten carbide are detected, whose conducting properties (see Table 2) redound to the improvement of the bulk electrical conductivity for this nanocomposite as compared to the carbon support. In brief, the great variety of supported nanoparticles may be considered to act as electrical switches either hindering or favouring the free electron transport between the AC cores of composite particles in contact under compression. Which of the two opposite behaviours occurs is ultimately determined by the intrinsic conductivity of the nanoparticle, which depends on its chemical nature and, thereby, on the metal oxide precursor and the heat treatment temperature.

Electron tunnelling is by far the predominant electrical transport mechanism in granular and powder carbon materials under compression. However, other additional and specific conduction mechanisms may also contribute to the bulk electrical conductivity of the hybrid materials, depending on the chemical nature of the supported nanoparticles. Among them, those concerning the various iron oxides have been the most widely investigated. Thus, several models have been described to explain the electrical conductivity in α-Fe_2O_3 under moderate compression; the most accepted one assumes conduction to take place primarily in the d levels of Fe^{3+} ions either with or without additional conduction in the sp-bands of oxide ions.[116,117] Kaneko *et al.* proposed a mechanism for the electrical transport in lightly compacted α-FeO(OH) powders involving the hopping of an electron from the t_{2g} orbital of a Fe^{2+} ion to the t_{2g} orbital of an adjacent Fe^{3+} ion, due to the slight overlapping of both orbitals.[118]

4. Conclusions

Two series of AC–metal oxide (Al_2O_3, Fe_2O_3, SnO_2, TiO_2, WO_3 and ZnO) nanocomposites were prepared by wet impregnation, oven-drying at 120 °C and subsequent heat treatment at 200 or 850 °C in an inert atmosphere. The electrical conductivity of AC and the resulting hybrid materials was studied under moderate compression. The mechanical properties of the nanocomposites are essentially determined by the carbon matrix. Both the decrease in volume and the increase in density under compression are only important at pressure values lower than 100 kPa for all samples. Unlike the mechanical properties, the bulk electrical conductivity of the hybrid materials is strongly influenced by the intrinsic conductivity, mean crystallite size, content and chemical nature of the supported nanoparticles, which ultimately depend on the metal oxide precursor and the heat treatment temperature. In this regard, for each precursor, conductivity improves with temperature rise due to the increase in the crystallite size and, in the case of Fe_2O_3, SnO_2 and WO_3 samples, to the formation of the corresponding metals in the elemental state and even metal carbides. Depending on their chemical nature, supported nanoparticles behave as electrical switches either hindering or favouring the free electron transport between the AC cores belonging to composite particles in contact under compression. Conductivity values measured for the nanocomposites are as a rule lower than those for AC, all of them falling in the range of semiconductor materials. Of the opposite effects of pressure and volume comprised in the variation of the conductivity with the mechanical work, the effect of pressure appears to predominate, as deduced from the slight resemblance between the plots of conductivity *versus* pressure and mechanical work.

Acknowledgements

Financial support by Gobierno de Extremadura and European FEDER Funds is gratefully acknowledged. A. Barroso-Bogeat thanks Spanish Ministerio de Educación, Cultura y Deporte for the concession of a FPU grant (AP2010-2574).

References

1 F. Rodríguez-Reinoso, *Carbon*, 1998, **36**, 159–175.
2 H. Jüntgen, *Fuel*, 1986, **65**, 1436–1446.
3 Y. Yang, K. Chiang and N. Burke, *Catal. Today*, 2011, **178**, 197–205.
4 P. Serp and J. L. Figueiredo, *Carbon Materials for Catalysis*, John Wiley & Sons, Hoboken, New Jersey, 2009.
5 M. Goyal, Nonenvironmental Industrial Applications of Activated Carbon Adsorption, in *Novel Carbon Adsorbents*, ed. J. M. D. Tascón, Elsevier, Amsterdam, 2012, pp. 605–638.
6 Q. Huang, X. Wang, J. Li, C. Dai, S. Gamboa and P. J. Sebastian, *J. Power Sources*, 2007, **164**, 425–429.
7 J. H. Park, O. O. Park, K. H. Shin, C. S. Jin and J. H. Kim, *Electrochem. Solid-State Lett.*, 2002, **5**, H7–H10.
8 M. Seredych, O. Mabayoje, M. M. Koleśnik, V. Krstić and T. J. Bandosz, *J. Mater. Chem.*, 2012, **22**, 7970–7978.
9 Q. L. Zhang, Y. C. Lin, X. Chen and N. Y. Gao, *J. Hazard. Mater.*, 2007, **148**, 671–678.
10 C. S. Castro, M. C. Guerreiro, M. Gonçalves, L. C. A. Oliveira and A. S. Anastácio, *J. Hazard. Mater.*, 2009, **164**, 609–614.
11 A. Guha, W. Lu, T. A. Zawodzinski Jr and D. A. Schiraldi, *Carbon*, 2007, **45**, 1506–1517.
12 M. Roosta, M. Ghaedi and M. Mohammadi, *Powder Technol.*, 2014, **267**, 134–144.
13 S. Pal, Y. Kyung Tak, J. Joardar, W. Kim, J. Eun Lee, M. Soo Han and J. Myong Song, *J. Nanosci. Nanotechnol.*, 2009, **9**, 2092–2103.
14 H. Tamai, U. Nobuaki and H. Yasuda, *Mater. Chem. Phys.*, 2009, **114**, 10–13.
15 P. Gorria, M. Sevilla, J. A. Blanco and A. B. Fuertes, *Carbon*, 2006, **44**, 1954–1957.
16 M. Qinghan, L. Ling, S. Huaihe and L. Licheng, *J. Mater. Sci.*, 2004, **39**, 3149–3150.
17 A. Barroso-Bogeat, C. Fernández-González, M. Alexandre-Franco and V. Gómez-Serrano, Activated carbon as a metal oxide support: a review, in *Activated Carbon: Classifications, Properties and Applications*, ed. J. F. Kwiatkowski, Nova Science Publishers, New York, 2011, pp. 297–318.
18 R. Sanjinés, M. D. Abad, C. Vâju, R. Smajda, M. Mionić and A. Magrez, *Surf. Coat. Technol.*, 2011, **206**, 727–733.
19 L. Wei and G. Yushin, *Nano Energy*, 2012, **1**, 552–565.
20 M. Zhi, C. Xiang, J. Li, M. Li and N. Wu, *Nanoscale*, 2013, **5**, 72–88.
21 Y. P. Wu, E. Rahm and R. Holze, *J. Power Sources*, 2003, **114**, 228–236.
22 S. Goriparti, E. Miele, F. De Angelis, E. Di Fabrizio, R. P. Zaccaria and C. Capligia, *J. Power Sources*, 2014, **257**, 421–443.
23 E. Antolini, *Appl. Catal., B*, 2009, **88**, 1–24.
24 V. V. Malyshev, *Russ. J. Phys. Chem. A*, 2009, **83**, 1940–1945.
25 Y. S. Kim, S. C. Ha, K. Kim, H. Yang, S. Y. Choi and Y. T. Kim, *Appl. Phys. Lett.*, 2005, **86**, 213105.
26 M. I. Baraton, L. Merhari, H. Ferkel and J. F. Castagnet, *Mater. Sci. Eng.*, 2002, **19**, 315–321.
27 A. V. Chadwick, R. M. Geatches and J. D. Wright, *Philos. Mag. A*, 1991, **64**, 999–1010.
28 T. Ates, C. Tatar and F. Yakuphanoglu, *Sens. Actuators, A*, 2013, **190**, 153–160.
29 M. I. Baraton and L. Merhari, *Mater. Res. Soc. Symp. Proc.*, 2004, **828**, 191–196.
30 S. Mrozowski, *Proceedings 3rd Biennal Carbon Conference*, Pergamon Press, Buffalo, 1957, p. 495.
31 R. Holm, *Electric contacts*, H. Geber, Stockholm, 1946.
32 R. Holm and E. Holm, *Electric contacts: theory and application*, Springer-Verlag, Berlin, 4th edn, 1967.
33 K. J. Euler, R. Kirchhof and H. Metzendorf, *Mater. Chem.*, 1979, **4**, 611–630.
34 C. Giraud, J. P. Clerc and E. Guyon, *Powder Technol.*, 1983, **35**, 107–111.
35 F. I. Zorin, *Inorg. Mater.*, 1986, **22**, 47–49.
36 N. Deprez and D. S. McLachlan, *J. Phys. D: Appl. Phys.*, 1988, **21**, 101–107.
37 A. Gervois, M. Ammi, T. Travers, D. Bideau, J. C. Messager and J. P. Troadec, *Physica A*, 1989, **157**, 565–569.
38 J. P. Troadec and D. Bideau, *Onde Electr.*, 1991, **71**, 30–33.
39 K. Kinoshita, *Carbon. Electrochemical and physicochemical properties*, Wiley, New York, 1988.
40 H. Braun and P. Herger, *Mater. Chem.*, 1982, **7**, 787–802.
41 J. Sánchez-González, A. Macías-García, M. F. Alexandre-Franco and V. Gómez-Serrano, *Carbon*, 2005, **43**, 741–747.
42 F. Skaupy and O. Kantrowicz, *Metallwirtsch., Metallwiss., Metalltech.*, 1931, **10**, 45–47.
43 A. Espinola, P. Mourente Miguel, M. Roedel Salles and A. Ribeiro Pinto, *Carbon*, 1986, **24**, 337–341.
44 A. Celzard, J. F. Marêché, F. Payot and G. Furdin, *Carbon*, 2002, **40**, 2801–2815.
45 K. J. Euler, *J. Power Sources*, 1978, **3**, 117–136.
46 B. Marinho, M. Ghislandi, E. Tkalya, C. E. Koning and G. De With, *Powder Technol.*, 2012, **221**, 351–358.
47 S. Marinkovic, C. Suznjevic and M. Djordjevic, *Phys. Status Solidi A*, 1971, **4**, 743–754.
48 J. A. Dodds, *J. Colloid Interface Sci.*, 1980, **77**, 317–327.
49 R. Ben Aïm and P. le Goff, *Powder Technol.*, 1968, **2**, 1–12.
50 J. P. Troadec, A. Gervois, D. Bideau and L. Oger, *J. Phys. C: Solid State Phys.*, 1987, **20**, 993–1004.
51 A. Bertei and C. Nicolella, *Powder Technol.*, 2011, **213**, 100–108.
52 A. Barroso-Bogeat, M. Alexandre-Franco, C. Fernández-González and V. Gómez-Serrano, *Fuel Process. Technol.*, 2014, **126**, 95–103.
53 A. Barroso-Bogeat, M. Alexandre-Franco, C. Fernández-González and V. Gómez-Serrano, *J. Mater. Sci. Technol.*, submitted.
54 B. D. Cullity, *Elements of X-ray diffraction*, Addison-Wesley, Reading, MA, 1959.
55 J. I. Langford and A. J. C. Wilson, *J. Appl. Crystallogr.*, 1978, **11**, 102–113.
56 J. M. Montes, F. G. Cuevas, J. Cintas and P. Urban, *Appl. Phys. A: Mater. Sci. Process.*, 2011, **105**, 935–947.
57 N. Tsuda, K. Nasu, A. Fujimori and K. Siratori, *Electronic Conduction in Oxides*, Springer, New York, 2nd edn, 2000.

58 W. T. Li, D. R. McKenzie, W. D. McFall, Q. C. Zhang and W. Wiszniewski, *Solid-State Electron.*, 2000, **44**, 1557–1562.
59 A. A. Akl, *Appl. Surf. Sci.*, 2004, **221**, 319–329.
60 N. Guskos, G. J. Papadopoulos, V. Likodimos, S. Patapis, D. Yarmis, A. Przepiera, K. Przepiera and J. Majszczyk, *Mater. Res. Bull.*, 2002, **37**, 1051–1061.
61 D. Reisinger, P. Majewski, M. Opel, L. Alff and R. Gross, *Appl. Phys. Lett.*, 2004, **85**, 4980.
62 A. V. Moholkar, S. M. Pawar, K. Y. Rajpure, C. H. Bhosale and J. H. Kim, *Appl. Surf. Sci.*, 2009, **255**, 9358–9364.
63 K. Krishnakumar, N. Pinna, K. Perumal and R. Jayaprakash, *AIP Conf. Proc.*, 2008, **1004**, 122–125.
64 K. W. Vogt, P. A. Kohl, W. B. Carter, R. A. Bell and L. A. Bottomley, *Surf. Sci.*, 1994, **301**, 203–213.
65 M. G. Hutchins, O. Abu-Alkhair, M. M. El-Nahass and K. Abdel-Hady, *J. Non-Cryst. Solids*, 2007, **353**, 4137–4142.
66 M. M. El-Nahass, H. A. M. Ali, M. Saadeldin and M. Zaghllol, *Physica B*, 2012, **407**, 4453–4457.
67 L. Beluze, J. C. Badot, R. Weil and V. Lucas, *J. Phys. Chem. B*, 2006, **110**, 7304–7308.
68 H. Wang, C. Li, H. Zhao, R. Li and J. Liu, *Powder Technol.*, 2013, **239**, 266–271.
69 F. G. de Souza Jr, J. A. Marins, J. C. Pinto, G. E. de Oliveira, C. M. Rodrigues and L. M. T. R. Lima, *J. Mater. Sci.*, 2010, **45**, 5012–5021.
70 E. A. Brandes and G. B. Brook, *Smithells Metals Reference Book*, Butterworth Heinemann, Oxford, 7th edn, 1992.
71 T. Dittrich, J. Weidmann, F. Koch, I. Uhlendorf and I. Lauermann, *Appl. Phys. Lett.*, 1999, **75**, 3980–3982.
72 H. O. Pierson, *Handbook of Chemical Vapour Deposition (CVD): Principles, Technology, and Applications*, William Andrew Inc., New York, 2nd edn, 1999.
73 S. Torquato and M. D. Rintoul, *Phys. Rev. Lett.*, 1995, **75**, 4067–4070.
74 S. J. Gregg and K. S. W. Sing, *Adsorption, surface area and porosity*, Academic Press, London, 2nd edn, 1982.
75 S. Brunauer, P. H. Emmet and E. Teller, *J. Am. Chem. Soc.*, 1938, **60**, 309–319.
76 M. M. Dubinin, in *Progress in Surface and Membrane Science*, ed. J. F. Danielli, M. D. Rosenberg and D. A. Cadenhead, Academic Press, New York, 1975, vol. 9, pp. 1–70.
77 D. Pantea, H. Darmstadt, S. Kaliaguine, L. Sümmchen and C. Roy, *Carbon*, 2001, **39**, 1147–1158.
78 M. Smisek and S. Cerny, *Active Carbon: Manufacture, Properties and Applications*, Elsevier, Amsterdam, 1979.
79 C. A. León y León, *Adv. Colloid Interface Sci.*, 1998, **76–77**, 341–372.
80 K. K. Nanda, *Phys. Lett. A*, 2012, **376**, 3301–3302.
81 W. D. Callister Jr, *Introducción a la Ciencia e Ingeniería de los Materiales*, Reverté, Barcelona, 1996, vol. 2.
82 L. J. Kennedy, J. Judith Vijaya and G. Sekaran, *Mater. Chem. Phys.*, 2005, **91**, 471–476.
83 T. Adinaveen, L. J. Kennedy, J. Judith Vijaya and G. Sekaran, *J. Ind. Eng. Chem.*, 2013, **19**, 1470–1476.
84 W. M. Daud, M. Badri and H. Mansor, *J. Appl. Phys.*, 1990, **67**, 1915–1917.
85 A. Barroso-Bogeat, M. Alexandre-Franco, C. Fernández-González, A. Macías-García and V. Gómez-Serrano, *Microporous Mesoporous Mater.*, 2014, DOI: 10.1016/j.micromeso.2014.07.023.
86 M. Koós, S. H. S. Moustafa, E. Szilágyi and I. Pócsik, *Diamond Relat. Mater.*, 1999, **8**, 1919–1926.
87 S. H. Moustafa, M. Koós and I. Pócsik, *J. Non-Cryst. Solids*, 1998, **227–230**, 1087–1091.
88 Y. Hishiyama, Y. Kaburagi and A. Ono, *Carbon*, 1979, **17**, 265–276.
89 Y. Inoue, M. Sugano, S. Kawakami, M. Kitano, K. Nakajima, H. Kato and M. Hara, *Bull. Chem. Soc. Jpn.*, 2013, **86**, 45–50.
90 J. B. Donnet, *Carbon*, 1994, **32**, 1305–1310.
91 G. D. Zhan and A. K. Mukherjee, *Int. J. Appl. Ceram. Technol.*, 2004, **1**, 161–171.
92 Y. Sakata, A. Muto, M. A. Uddin, M. Tanihara, K. Harino, J. Takada and Y. Kusano, *J. Jpn. Soc. Powder Powder Metall.*, 1998, **45**, 806–811.
93 Y. Zhu, L. Zhang, F. M. Schappacher, R. Pöttgen, J. Shi and S. Kaskel, *J. Phys. Chem. C*, 2008, **112**, 8623–8628.
94 Y. Liu and H. Yan, *Mater. Lett.*, 2011, **65**, 1063–1065.
95 Y. Ao, J. Xu, X. Shen, D. Fu and C. Yuan, *J. Hazard. Mater.*, 2008, **160**, 295–300.
96 C. S. Castro, M. C. Guerreiro, M. Gonçalves, L. C. A. Oliveira and A. S. Anastácio, *J. Hazard. Mater.*, 2009, **164**, 609–614.
97 Q. L. Zhang, Y. C. Lin, X. Chen and N. Y. Gao, *J. Hazard. Mater.*, 2007, **148**, 671–678.
98 A. Quintanilla, N. Menéndez, J. Tornero, J. A. Casas and J. J. Rodríguez, *Appl. Catal., B*, 2008, **81**, 105–114.
99 K. L. López-Maldonado, P. de la Presa, M. A. de la Rubia, P. Crespo, J. de Frutos, A. Hernando, J. A. Matutes Aquino and J. T. Elizalde Galindo, *J. Nanopart. Res.*, 2014, **16**, 2482.
100 S. L. Patil, M. A. Chougule, S. G. Pawar, B. T. Raut, S. Sen and V. B. Patil, *J. Alloys Compd.*, 2011, **509**, 10055–10061.
101 M. J. Iqbal, N. Yaqub, B. Sepiol and B. Ismail, *Mater. Res. Bull.*, 2011, **46**, 1837–1842.
102 N. Ponpandian and A. Narayanasamy, *J. Appl. Phys.*, 2002, **92**, 2770–2778.
103 N. Tigau, V. Ciupina, G. Prodan, G. I. Rusu, C. Gheorghies and E. Vasile, *J. Optoelectron. Adv. Mater.*, 2003, **5**, 907–912.
104 R. S. Rao, A. B. Walters and M. A. Vannice, *J. Phys. Chem. B*, 2005, **109**, 2086–2092.
105 R. N. Viswanath and S. Ramasamy, *Colloids Surf., A*, 1998, **133**, 49–56.
106 A. W. Czanderna, C. N. Ramachandra Rao and J. M. Honig, *Trans. Faraday Soc.*, 1958, **54**, 1069–1073.
107 B. Tryba, A. W. Morawski and M. Inagaki, *Appl. Catal., B*, 2003, **41**, 427–433.
108 Y. Li, S. Zhang, Q. Yu and W. Yin, *Appl. Surf. Sci.*, 2007, **253**, 9254–9258.
109 Y. X. Chen, B. H. Luo, B. Y. Zhao, Y. J. Lai, H. Z. Wang, M. Y. Gao, W. X. Zhang and K. B. Chen, *J. Inorg. Organomet. Polym.*, 2012, **22**, 90–96.

110 N. Probst and E. Grivei, *Carbon*, 2002, **40**, 201–205.
111 D. Pantea, H. Darmstadt, S. Kaliaguine, S. Blacher and C. Roy, *Rubber Chem. Technol.*, 2002, **75**, 691–700.
112 J. M. Montes, F. G. Cuevas and J. Cintas, *Metall. Mater. Trans. B*, 2007, **38**, 957–964.
113 J. M. Montes, F. G. Cuevas and J. Cintas, *Granular Matter*, 2011, **13**, 439–446.
114 T. J. Garino, *J. Mater. Res.*, 2002, **17**, 2691–2697.
115 P.-G. De Gennes, *Europhys. Lett.*, 1996, **35**, 145–149.
116 F. J. Morin, *Phys. Rev.*, 1954, **93**, 1195–1199.
117 E. Knittle and R. Jeanloz, *Solid State Commun.*, 1986, **58**, 129–131.
118 K. Kaneko and K. Inouye, *Bull. Chem. Soc. Jpn.*, 1974, **47**, 1139–1142.